



Research paper

Force and time-optimal trajectory planning for dual-arm unilateral cooperative grasping

Roberto Di Leva^a, Hubert Gatttringer^b, Andreas Müller^b, Marco Carricato^{a,*}^a Department of Industrial Engineering - University of Bologna, Viale del Risorgimento 2, Bologna, 40136, Italy^b Institute of Robotics - Johannes Kepler University Linz, Altenberger Straße 69, Linz, 4040, Austria

ARTICLE INFO

Keywords:

Dual-arm manipulation
Cooperative grasping
Time-optimal trajectory planning
Admittance control
Collaborative robotics

ABSTRACT

This paper studies the dual-arm manipulation of an object by means of two collaborative robots. The latter hold the object through limited contact areas, thus applying unilateral contact constraints. This manipulation strategy increases versatility, since it does not require specific grippers depending on the object shape and size. However, to ensure grasping stability (i.e. no slipping of the object), a suitable internal force must be prescribed to ensure the fulfillment of the static-friction condition. In this work, the trend of the internal force is included among the inputs of a time-optimal trajectory planning, in order to find the minimal internal prestress that is able to both satisfy the static-friction condition and manipulate the object in minimal time. Admittance control is used to modulate the forces exerted by the robot end-effectors on the object. An extensive experimentation, on different 6-dimensional trajectories reaching linear and angular accelerations up to 4.5 m/s^2 and 7.4 rad/s^2 , is presented and discussed.

1. Introduction

The increasing need for robots operating side by side with humans in industrial scenarios often requires dual-arm setups [1], in which two robots manipulate the same object. This way, the dual-arm robotic system is able to replicate the operator's bi-manual skills, which can be crucial in shared tasks or in view of inserting robots in environments originally intended for humans [2]. Moreover, the closed kinematic chain of dual-arm setups combines the stiffness and strength of a parallel manipulator with the versatility and dexterity of a serial manipulator. The latter characteristics can be exploited especially when the objects to manipulate are bulky or too heavy for a single-arm robot. This is the case of automotive processing lines, and also of emerging e-commerce packaging lines [3], in which cuboids constitute the vast majority of items stored in warehouses.

Depending on the type of interaction between the robot end-effectors and the object, two types of cooperative tasks may be identified [4]:

- *the cooperative robots hold the object through bilateral grasp surfaces*, namely the object is rigidly grasped by each robot (e.g. using a gripper), which implies that no relative motion can occur at the interaction surfaces;
- *the cooperative robots hold the object through unilateral contact surfaces*: in this case, relative motion between each end-effector and the object may occur, due to the fact that contact constraints are unilateral; accordingly, a pulling force may result in slipping of the object and hence in contact loss.

* Correspondence to: Viale del Risorgimento 2, 40136, Bologna, Italy.

E-mail address: marco.carricato@unibo.it (M. Carricato).

O	origin of the inertial frame F_0
B	object center of mass (COM)
F_b	frame attached to the object and centered in B
$\mathbf{r} \in \mathbb{R}^3$	position vector between O and B
$\mathbf{R} \in \mathbb{R}^{3 \times 3}$	rotation matrix between F_0 and F_b
$m_b, \boldsymbol{\Theta}_B \in \mathbb{R}^{3 \times 3}$	object mass and inertia matrix
$\dot{\mathbf{r}} \in \mathbb{R}^3, \ddot{\mathbf{r}} \in \mathbb{R}^3$	object velocity and acceleration
$\boldsymbol{\omega} \in \mathbb{R}^3, \dot{\boldsymbol{\omega}} \in \mathbb{R}^3$	object angular velocity and acceleration
l/r	subscript indicating the left/right robot
$\mathbf{h}_b = [\mathbf{f}_b^T \ \mathbf{t}_b^T]^T \in \mathbb{R}^6$	net wrench on the object
$\mathbf{h}_l = [\mathbf{f}_l^T \ \mathbf{t}_l^T]^T \in \mathbb{R}^6$	wrench applied by the left robot on the object
$\mathbf{h}_r = [\mathbf{f}_r^T \ \mathbf{t}_r^T]^T \in \mathbb{R}^6$	wrench applied by the right robot on the object
E_l/E_r	centers of the circular contact areas between the robots and the object
F_l	frame attached to the object at E_l
$\{\mathbf{f}_l\}_l = [f_{l,Tx} \ f_{l,Ty} \ f_{l,N}]^T$	projection of the force \mathbf{f}_l on F_l
$\{\mathbf{f}_r\}_l = [f_{r,Tx} \ f_{r,Ty} \ f_{r,N}]^T$	projection of the force \mathbf{f}_r on F_l
f_p	internal force
s, \dot{s}, \ddot{s}	motion law of the path parameter
$\mathbf{u} \in \mathbb{R}^2$	control input of the optimization
$\mathbf{x} \in \mathbb{R}^{18}$	system state of the optimization
$\mathbf{q}_l/\mathbf{q}_r \in \mathbb{R}^6$	left/right robot joint coordinates
$\mathbf{J}_l/\mathbf{J}_r \in \mathbb{R}^{6 \times 6}$	left/right robot Jacobian matrix
$\xi_l/\xi_r \in \mathbb{R}^6$	left/right robot end-effector twists
t_e	final time of the generic trajectory

The latter strategy, which will be hereafter referred to as *unilateral cooperative grasping* (sometimes also called *palm-grasping* [5,6]), has been seldom studied in the literature, though it presents some benefits compared to gripper-based manipulation, namely the smaller investment costs (since specialized grippers are spared) and a higher versatility with respect to (w.r.t.) uncertainties in the object shape and size. In fact, grabbing an object with a gripper requires *ad hoc* geometric features, and the object needs to be small enough to be hosted within the stroke of the gripper fingers. However, in the scenario of unilateral cooperative grasping, dual-arm manipulation is achieved only if a stable grasp is ensured, i.e. no slipping of the object occurs [6,7]. To this aim, the normal and tangential forces that the robots exert on the object must fall inside the static-friction cone.

Once the desired contact forces are computed, the most suitable force-control strategy must be chosen. In fact, in the context of dual-arm manipulation, each robot cannot apply a force on the manipulated object without being concerned of the action performed by the other robot. Compliant control can be divided into two categories [8]: direct force control [9,10], and indirect force control [11]. In the context of the former strategy, parallel force/position control represents the most viable alternative to accomplish the dual-arm task, thanks to its robustness to uncertainties. In this scenario, the *primary* robot is position-controlled, whereas the other one (*secondary*) is controlled through parallel force/position control. A primary–secondary strategy is adopted in [12], but only motions with low dynamics are considered and no direct mention is made to the computation of the desired internal force necessary to stably and safely grasp the objects. However, in the case of unilateral cooperative grasping, the contact stability may be invalidated by the fact that the primary robot follows the desired trajectory while the secondary one has to chase it and simultaneously apply an internal force on the object to avoid slipping. For this reason, indirect force control, which allows the two manipulators to be controlled at the same hierarchy level, seems a more robust option for unilateral cooperative grasping, in the form of either impedance or admittance control.

In [13], cooperative grasping is pursued by adopting a centralized impedance control aimed at obtaining a compliant behavior at the object level, and a decentralized impedance control at the end-effector level, aimed at avoiding large internal load on the object. Even in this case the described experiments do not consider highly dynamical motions (the task duration settles around 115 s, and the position and angular excursions are limited) and no clear clue seems to be given regarding how slipping is avoided during task execution. In [14], the impedance control of two 7-DOF cobots is implemented at three levels: at the object level to control the interaction forces between the object and the environment, at the end-effector level to control the internal forces exerted on the object, and finally at body level to limit contact between the robots and the environment. The desired internal force is arbitrarily set, and the whole algorithm is only verified in a simulation scenario. Fast trajectories are executed in [15], with the two cobots being admittance-controlled. Linear velocities up to 0.4 m/s are claimed, but no details are given about the performed trajectories (i.e., the maximum acceleration reached, the angular velocities and accelerations, the exchanged forces). In this case too, the authors do not clarify the method adopted to avoid the object slipping during motion.

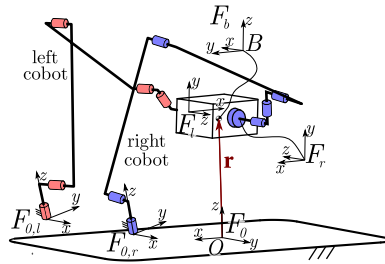


Fig. 1. Dual-arm unilateral cooperative grasping.

More recently, the problem of time-optimal unilateral cooperative grasping, aimed at performing the dual-arm task in minimal time, is addressed in [16], by adopting admittance control of two industrial robots. In this case, the internal force, aimed at enabling grasping stability, is achieved by prescribing a *constant virtual penetration* on the object; however, the penetration value is not optimized and it is chosen on a trial-and-error basis. Experiments show that slipping may occur for highly dynamical motions. In [17], the time-optimal path-tracking problem for dual-arm manipulation is formulated, considering the optimal trend of the internal force. Simulations of highly dynamical motions are provided, but they are purely illustrative, with dynamic parameters not adhering to a real case. Moreover, no experiments on real robots are presented. The same type of unilateral cooperative grasping is studied in [6,7], with the aim of dynamically adjusting the internal force or slowing down the motion to satisfy friction-cone conditions; however, experiments only present low-dynamics trajectories.

In this paper, we opt for admittance control of the two robots, since it provides the direct translation of a force input into a command at motion level, which represents a standard practice in industrial robot control. Moreover, the internal force, as well as the path parameter defining the time performance of the trajectory, are chosen as independent variables to be optimized, provided that the friction-cone constraint is enforced. This way the solution of the problem leads to the optimal motion and optimal internal-force profiles that the two robots have to apply to keep the contact forces inside the friction cone, while at the same time guaranteeing the shortest trajectory duration compatible with this constraint. The main aim of the paper is to verify the effectiveness of the proposed optimization approach in accomplishing the dual-arm task by unilateral grasping, while the manipulated object follows general 6D trajectories, executed with maximum linear and angular accelerations up to 4.5 m/s^2 and 7.4 rad/s^2 , respectively. In particular, the distinctive contributions of the paper are the following:

- The considered motions are highly dynamical and 6D, hence including the orientation change of the manipulated object.
- An extensive experimental campaign is performed and discussed, making the manipulated object follow 6D trajectories with maximum linear velocities and accelerations up to 0.6 m/s and 4.5 m/s^2 , and angular velocities and accelerations up to 1.1 rad/s and 7.4 rad/s^2 , respectively (these limits mainly depend on the hardware at our disposal, see Section 5.2).
- The force distribution among the two robots is experimentally analyzed to prove the fulfillment of the friction constraints during trajectory execution and to verify the correct application of the net wrench on the object. To the best of the authors' knowledge, such a broad experimental study of dynamical 6D motions in case of unilateral cooperative grasping is presented for the first time.

The following assumptions are made throughout the paper:

- the manipulated object has a parallelepiped-like shape;
- the contact between the robots and the object occurs on circular flat surfaces;
- the only external force applied on the manipulated object is gravity;
- the mass and inertia matrix of the object are known.

The latter assumption is plausible in structured environments such as e-commerce packaging lines. Moreover, inertia-parameter estimation lies outside the scope of the paper, and the authors suggest referring to [18,19] for details about suitable estimation procedures.

The structure of the paper is as follows. Section 2 describes the model employed for the determination of the forces exerted on the object. Section 3 presents the time and force optimization problem. Section 4 provides details about the adopted control strategy. Section 5 illustrates the setup used for the experiments and the corresponding results. Finally, Section 6 draws conclusions and gives suggestions for future developments.

2. Dynamic model

The object trajectory is prescribed in terms of:

- the position $\mathbf{r}(t)$, where \mathbf{r} is the position vector connecting the origin O of the inertial frame F_0 to the object center of mass (COM) B (Fig. 1);

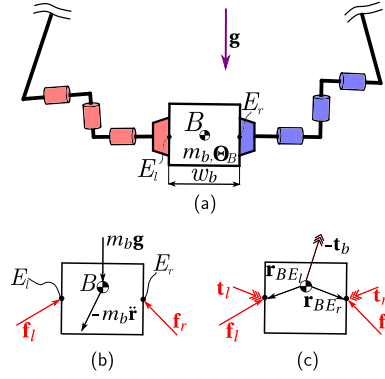


Fig. 2. Dynamic equilibrium of the object: (a) Front view; (b) Force equilibrium; (c) Moment equilibrium.

- the orientation $\mathbf{R}(t)$, with \mathbf{R} being the rotation matrix between F_0 and the frame F_b attached to the object in B (Fig. 1).

The object motion is achieved as long as the following net wrench $\mathbf{h}_b = [\mathbf{f}_b^T \mathbf{t}_b^T]^T$ is exerted on the object:

$$\mathbf{f}_b = -m_b \mathbf{g} + m_b \ddot{\mathbf{r}}, \quad (1a)$$

$$\mathbf{t}_b = \boldsymbol{\Theta}_B \dot{\boldsymbol{\omega}} + \tilde{\boldsymbol{\omega}} \boldsymbol{\Theta}_B \boldsymbol{\omega}, \quad (1b)$$

where m_b is the mass of the object, $\boldsymbol{\Theta}_B$ is its inertia matrix w.r.t. the COM B , $\boldsymbol{\omega}$ is the angular velocity, and \mathbf{g} is the gravity acceleration, whose expression in frame F_0 is $\{\mathbf{g}\}_0 = [0 \ 0 \ -g]^T$. We denote the projection of a 3-dimensional vector on a generic frame F_j as $\{\cdot\}_j$, whereas the symbol \sim denotes its skew-symmetric representation. For the object equilibrium, the wrenches $\mathbf{h}_l = [\mathbf{f}_l^T \mathbf{t}_l^T]^T$ and $\mathbf{h}_r = [\mathbf{f}_r^T \mathbf{t}_r^T]^T$, respectively exerted by the *left* and the *right* robot on the object, must produce the desired net wrench, namely (Fig. 2):

$$\mathbf{f}_l + \mathbf{f}_r = -m_b \mathbf{g} + m_b \ddot{\mathbf{r}}, \quad (2a)$$

$$\mathbf{t}_l + \mathbf{t}_r + \tilde{\mathbf{r}}_{BE_l} \mathbf{f}_l + \tilde{\mathbf{r}}_{BE_r} \mathbf{f}_r = \boldsymbol{\Theta}_B \dot{\boldsymbol{\omega}} + \tilde{\boldsymbol{\omega}} \boldsymbol{\Theta}_B \boldsymbol{\omega}, \quad (2b)$$

where E_l and E_r are the centers of the circular contact areas between the robots and the object.

The object equilibrium can be written in compact form as:

$$\mathbf{W} \mathbf{h}_{l,r} = \mathbf{h}_b, \quad (3)$$

where $\mathbf{h}_{l,r} = [\mathbf{h}_l^T \ \mathbf{h}_r^T]^T = [\mathbf{f}_l^T \ \mathbf{t}_l^T \ \mathbf{f}_r^T \ \mathbf{t}_r^T]^T \in \mathbb{R}^{12}$ and $\mathbf{W} \in \mathbb{R}^{6 \times 12}$ is the grasp matrix

$$\mathbf{W} = \begin{bmatrix} \mathbf{I} & \mathbf{0} & \mathbf{I} & \mathbf{0} \\ \tilde{\mathbf{r}}_{BE_l} & \mathbf{I} & \tilde{\mathbf{r}}_{BE_r} & \mathbf{I} \end{bmatrix}, \quad (4)$$

with $\mathbf{I} \in \mathbb{R}^{3 \times 3}$ being the identity matrix. Since the problem contains 12 scalar unknowns $\mathbf{h}_{l,r}$ in the 6 scalar equations (3), its solution is under-determined, so that:

$$\mathbf{h}_{l,r} = \mathbf{W}^\dagger \mathbf{h}_b + \mathbf{V} \mathbf{h}_p. \quad (5)$$

Here, $\mathbf{W}^\dagger = \mathbf{G} \mathbf{W}^T (\mathbf{W} \mathbf{G} \mathbf{W}^T)^{-1} \in \mathbb{R}^{12 \times 6}$ is a pseudo-inverse of \mathbf{W} [20], whose weighting matrix is \mathbf{G} , and $\mathbf{V} \in \mathbb{R}^{12 \times 6}$ is an orthogonal complement matrix such that $\mathbf{W} \mathbf{V} = \mathbf{0}$. Additionally, $\mathbf{h}_p = [\mathbf{f}_p^T \ \mathbf{t}_p^T]^T$ represents a desired wrench that generates *internal prestressing*. The way the two robots distribute the wrenches \mathbf{h}_l and \mathbf{h}_r on the object is influenced by the weighting matrix \mathbf{G} . If, according to [21], \mathbf{G} is chosen as:

$$\mathbf{G} = \begin{bmatrix} \mathbf{0} & \mathbf{I} & \mathbf{0} & \mathbf{0} \\ \mathbf{I} & \mathbf{0} & \mathbf{0} & \mathbf{0} \\ \mathbf{0} & \mathbf{0} & \mathbf{0} & \mathbf{I} \\ \mathbf{0} & \mathbf{0} & \mathbf{I} & \mathbf{0} \end{bmatrix}, \quad (6)$$

the pseudo-inverse \mathbf{W}^\dagger becomes

$$\mathbf{W}^\dagger = \begin{bmatrix} \frac{1}{2} \mathbf{I} & \mathbf{0} \\ -\frac{1}{2} \tilde{\mathbf{r}}_{BE_l} & \frac{1}{2} \mathbf{I} \\ \frac{1}{2} \mathbf{I} & \mathbf{0} \\ -\frac{1}{2} \tilde{\mathbf{r}}_{BE_r} & \frac{1}{2} \mathbf{I} \end{bmatrix}. \quad (7)$$

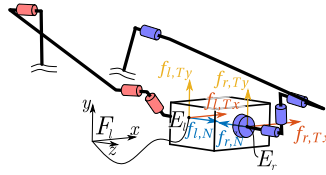


Fig. 3. Projection of the forces \mathbf{f}_l and \mathbf{f}_r on the coordinate frame F_l .

The orthogonal complement matrix \mathbf{V} can be chosen as

$$\mathbf{V} = \begin{bmatrix} \mathbf{I} & \mathbf{0} \\ -\tilde{\mathbf{r}}_{BE_l} & \mathbf{I} \\ -\mathbf{I} & \mathbf{0} \\ \tilde{\mathbf{r}}_{BE_r} & -\mathbf{I} \end{bmatrix}, \quad (8)$$

with its pseudo-inverse \mathbf{V}^\dagger (needed in Section 4) being

$$\mathbf{V}^\dagger = \frac{1}{2} \begin{bmatrix} \mathbf{I} & \mathbf{0} & -\mathbf{I} & \mathbf{0} \\ \tilde{\mathbf{r}}_{BE_l} & \mathbf{I} & -\tilde{\mathbf{r}}_{BE_r} & -\mathbf{I} \end{bmatrix}. \quad (9)$$

Finally, from Eqs. (5), (7) and (8), the expressions of \mathbf{f}_l , \mathbf{t}_l , \mathbf{f}_r and \mathbf{t}_r become

$$\mathbf{f}_l = \frac{1}{2}(-m_b \mathbf{g} + m_b \ddot{\mathbf{r}}) + \mathbf{f}_p, \quad (10a)$$

$$\mathbf{t}_l = \frac{1}{2}(\boldsymbol{\Theta}_B \dot{\boldsymbol{\omega}} + \tilde{\boldsymbol{\omega}} \boldsymbol{\Theta}_B \boldsymbol{\omega}) - \tilde{\mathbf{r}}_{BE_l} \left(\frac{1}{2} \mathbf{f}_b + \mathbf{f}_p \right) + \mathbf{t}_p, \quad (10b)$$

$$\mathbf{f}_r = \frac{1}{2}(-m_b \mathbf{g} + m_b \ddot{\mathbf{r}}) - \mathbf{f}_p, \quad (10c)$$

$$\mathbf{t}_r = \frac{1}{2}(\boldsymbol{\Theta}_B \dot{\boldsymbol{\omega}} + \tilde{\boldsymbol{\omega}} \boldsymbol{\Theta}_B \boldsymbol{\omega}) - \tilde{\mathbf{r}}_{BE_r} \left(\frac{1}{2} \mathbf{f}_b - \mathbf{f}_p \right) - \mathbf{t}_p. \quad (10d)$$

Eqs. (10) represent an equal distribution of the reaction forces among the robot end-effectors. In particular, Eqs. (10a) and (10c) imply that each robot applies half of the net force \mathbf{f}_b necessary to guide the object along its desired trajectory, besides the prestress \mathbf{f}_p . Regarding Eqs. (10b) and (10d), in general, no internal grasp torque is desired, implying $\mathbf{t}_p = \mathbf{0}$.

Another suitable coordinate frame F_l can be attached to the object at E_l . F_l is oriented so that its z -axis points towards the pushing direction of the left robot on the object, while the other two axes, e.g., the x and y axes, are oriented as depicted in Fig. 3. We assume that the only nonzero component of the internal prestress is along the z -axis of frame F_l , so that $\{\mathbf{f}_p\}_l = [0 \ 0 \ f_p]^T$. The projections of forces \mathbf{f}_l and \mathbf{f}_r on F_l are composed of tangential components along the x and y directions and by a normal component along the z -axis (Fig. 3). Taking advantage of Eqs. (10a) and (10c), such projections are equal to:

$$\{\mathbf{f}_l\}_l = \begin{bmatrix} f_{l,Tx} \\ f_{l,Ty} \\ f_{l,N} \end{bmatrix} = \frac{m_b}{2} \begin{bmatrix} g_x + \ddot{r}_x \\ g_y + \ddot{r}_y \\ g_z + \ddot{r}_z \end{bmatrix} + \begin{bmatrix} 0 \\ 0 \\ f_p \end{bmatrix}, \quad (11a)$$

$$\{\mathbf{f}_r\}_l = \begin{bmatrix} f_{r,Tx} \\ f_{r,Ty} \\ f_{r,N} \end{bmatrix} = \frac{m_b}{2} \begin{bmatrix} g_x + \ddot{r}_x \\ g_y + \ddot{r}_y \\ g_z + \ddot{r}_z \end{bmatrix} - \begin{bmatrix} 0 \\ 0 \\ f_p \end{bmatrix}. \quad (11b)$$

The above dynamic model holds as far as none of the two robots loses contact with the manipulated object, i.e. there is no slipping of the latter. If the internal prestress is not taken into account, the solution of Eq. (11) may lead to a contact force \mathbf{f}_j (with $j = l, r$) pulling away from the object. Accordingly, the prestress force \mathbf{f}_p has two roles. On the one hand, it must make the normal-force components $f_{l,N}$ and $f_{r,N}$, respectively, positive and negative (so that both \mathbf{f}_l and \mathbf{f}_r push on the object). On the other hand, it must make the friction-cone condition satisfied on both sides of the contact, namely:

$$f_{l,N} > 0, \quad (12a)$$

$$f_{r,N} < 0, \quad (12b)$$

$$\sqrt{f_{j,Tx}^2 + f_{j,Ty}^2} \leq \mu |f_{j,N}|, \quad j = l, r, \quad (12c)$$

with μ being the static friction coefficient between the robot extremities and the object. In other words, the internal prestress f_p has to make the normal force $|f_{j,N}|$ large enough to satisfy the friction-cone condition on both sides of the contact ($j = l, r$), but at

the same time, it needs to be bounded to avoid damage to the object. These conditions cannot be satisfied by adopting conventional motion-planning techniques that do not optimize force application on the object.

Other anti-slipping constraints emerge from the consideration that the contact torques $t_{l,N}$ and $t_{r,N}$ around the z -axis of F_l cannot be arbitrarily large [22]. Indeed, the highest value of the local frictional torque $dt_{j,\mu}$ ($j = l, r$) can be computed as the highest local frictional force $df_{j,\mu} = \mu p_j dA$ times the distance ρ between the center of the contact disc and the infinitesimal area dA :

$$dt_{j,\mu} = df_{j,\mu} \rho = \mu p_j dA \rho, \quad j = l, r, \quad (13)$$

where the pressure distribution p_j is assumed to be uniform and equal to $p_j = \frac{f_{j,N}}{\pi R^2}$, $dA = \rho d\rho d\phi$ is the infinitesimal area of the contact disc and R is the radius of the latter. The largest total frictional torque is hence the integral on the whole contact surface:

$$t_{j,\mu} = \mu \frac{f_{j,N}}{\pi R^2} \int_0^{2\pi} \int_0^R \rho^2 d\rho d\phi = \frac{2}{3} \mu R |f_{j,N}|, \quad j = l, r. \quad (14)$$

Accordingly, it must be:

$$|t_{j,N}| \leq \frac{2}{3} \mu R |f_{j,N}|, \quad j = l, r. \quad (15)$$

Notice that t_l and t_r depend on the location of the object COM B with respect to E_l and E_r . We assume that, due to a suitable trajectory planning, E_r is kept aligned with the z -axis of F_l , whereas a certain misalignment is allowed for B . However, for the sake of simplicity, B is assumed to always lie in the median plane of the object. Accordingly:

$$\{\mathbf{r}_{BE_l}^T\}_l = \begin{bmatrix} e_x & e_y & -\frac{w_b}{2} \end{bmatrix}^T, \quad (16a)$$

$$\{\mathbf{r}_{BE_r}^T\}_l = \begin{bmatrix} e_x & e_y & \frac{w_b}{2} \end{bmatrix}^T, \quad (16b)$$

where e_x and e_y are the misalignments of B along the x and y axes of F_l , respectively, and w_b is the object width. Misalignments e_x, e_y may have a useful role in accounting for the uncertainties on the object-COM position w.r.t. the location of the contact surfaces.

It is worth emphasizing that, since the contact surfaces in our model have finite dimensions (see Fig. 3), the resulting grasp involves both form-closure and force-closure [23]. Indeed, since the contact discs are parallel to the xy -plane of F_l , the manipulated object can neither translate along the z -axis of F_l , nor rotate about any direction perpendicular to it. Accordingly, the only possible movements are ‘slipping’ motions, namely rotations about lines parallel to z -axis of F_l and translations on the xy -plane of F_l . These ‘slipping’ motions are prevented if the force-closure conditions, represented by (12) and (15), are fulfilled, hence ensuring grasping stability [6,7].

3. Time-optimal trajectory planning

3.1. Trajectory definition

The path of the object COM and the Euler angles $\theta = [\theta_x \ \theta_y \ \theta_z]^T$ used to describe the object orientation (e.g., the rotation matrix \mathbf{R} between frames F_0 and F_b) are parameterized in terms of the parameter s :

$$\mathbf{r} = \mathbf{r}(s), \quad s \in [0, 1], \quad (17a)$$

$$\theta = \theta(s), \quad s \in [0, 1]. \quad (17b)$$

Both \mathbf{r} and θ can be defined by a suitable number of B-splines [24,25]:

$$\mathbf{r}(s) = \sum_{j=0}^m B_j^d(s) \mathbf{p}_j, \quad s \in [0, 1], \quad (18a)$$

$$\theta(s) = \sum_{j=0}^m B_j^d(s) \mathbf{o}_j, \quad s \in [0, 1], \quad (18b)$$

where B_j^d are B-spline basis functions of degree d , \mathbf{p}_j are $m+1$ control points and \mathbf{o}_j are the $m+1$ angular control points. The motion law of the path parameter $s(t)$ allows the trajectory to be defined as

$$\dot{\mathbf{r}}(s, \dot{s}) = \mathbf{r}'(s) \dot{s}, \quad (19a)$$

$$\ddot{\mathbf{r}}(s, \dot{s}, \ddot{s}) = \mathbf{r}''(s) \dot{s}^2 + \mathbf{r}'(s) \ddot{s}, \quad (19b)$$

$$\dot{\theta}(s, \dot{s}) = \theta'(s) \dot{s}, \quad (20a)$$

$$\ddot{\theta}(s, \dot{s}, \ddot{s}) = \theta''(s) \dot{s}^2 + \theta'(s) \ddot{s}, \quad (20b)$$

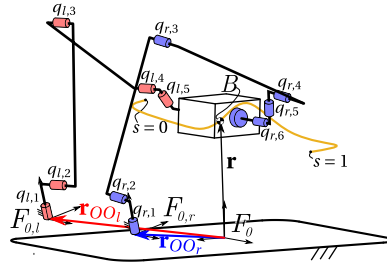


Fig. 4. Dual-arm trajectory planning.

with $()' = \partial()/\partial s$ denoting the derivative w.r.t. s .

The relation between the angular velocity and acceleration $\omega, \dot{\omega}$ and the time derivatives of the Euler angles is given by the expressions:

$$\omega = \mathbf{A}\dot{\theta}, \quad (21a)$$

$$\dot{\omega} = \mathbf{A}\ddot{\theta} + \dot{\mathbf{A}}\dot{\theta}, \quad (21b)$$

with matrix \mathbf{A} depending on the orientation representation and the frame on which ω and $\dot{\omega}$ are projected. In our case, choosing the XYZ Euler-angle representation and projecting vectors on frame F_0 , we have:

$$\mathbf{A} = \begin{bmatrix} 1 & 0 & \sin \theta_y \\ 0 & \cos \theta_x & -\sin \theta_x \cos \theta_y \\ 0 & \sin \theta_x & \cos \theta_x \cos \theta_y \end{bmatrix}. \quad (22)$$

3.2. Force limits

Once the motion of the object is written in terms of the path parameter s and its time derivatives \dot{s}, \ddot{s} , the contact forces in Eqs. (11a), (11b) can be expressed as a function of the motion law, that is:

$$\begin{bmatrix} f_{l,Tx}(s, \dot{s}, \ddot{s}) \\ f_{l,Ty}(s, \dot{s}, \ddot{s}) \\ f_{l,N}(s, \dot{s}, \ddot{s}, f_p) \end{bmatrix} = \frac{m_b}{2} \begin{bmatrix} g_x(s) + \ddot{r}_x(s, \dot{s}, \ddot{s}) \\ g_y(s) + \ddot{r}_y(s, \dot{s}, \ddot{s}) \\ g_z(s) + \ddot{r}_z(s, \dot{s}, \ddot{s}) \end{bmatrix} + \begin{bmatrix} 0 \\ 0 \\ f_p \end{bmatrix}, \quad (23a)$$

$$\begin{bmatrix} f_{r,Tx}(s, \dot{s}, \ddot{s}) \\ f_{r,Ty}(s, \dot{s}, \ddot{s}) \\ f_{r,N}(s, \dot{s}, \ddot{s}, f_p) \end{bmatrix} = \frac{m_b}{2} \begin{bmatrix} g_x(s) + \ddot{r}_x(s, \dot{s}, \ddot{s}) \\ g_y(s) + \ddot{r}_y(s, \dot{s}, \ddot{s}) \\ g_z(s) + \ddot{r}_z(s, \dot{s}, \ddot{s}) \end{bmatrix} - \begin{bmatrix} 0 \\ 0 \\ f_p \end{bmatrix}. \quad (23b)$$

By substituting Eqs. (23) inside inequalities (12) and (15), the no-slipping conditions for both robots can be written as functions of the motion law (s, \dot{s}, \ddot{s}) and the internal force f_p , namely as:

$$\frac{m_b}{2}(g_z + \ddot{r}_z) + f_p > 0, \quad (24a)$$

$$\frac{m_b}{2}(g_z + \ddot{r}_z) - f_p < 0, \quad (24b)$$

$$f_{l,Tx}^2 + f_{l,Ty}^2 \leq \mu^2 \left(\frac{m_b}{2}(g_z + \ddot{r}_z) + f_p \right)^2, \quad (24c)$$

$$f_{r,Tx}^2 + f_{r,Ty}^2 \leq \mu^2 \left(\frac{m_b}{2}(g_z + \ddot{r}_z) - f_p \right)^2, \quad (24d)$$

$$t_{l,N}^2 \leq \frac{4}{9} \mu^2 R^2 \left(\frac{m_b}{2}(g_z + \ddot{r}_z) + f_p \right)^2, \quad (25a)$$

$$t_{r,N}^2 \leq \frac{4}{9} \mu^2 R^2 \left(\frac{m_b}{2}(g_z + \ddot{r}_z) - f_p \right)^2. \quad (25b)$$

The fulfillment of the friction inequalities ((24), (25)) requires a trade-off between the fastest motion law and the internal prestress able to avoid slipping of the object. This suggests that the optimization problem can be represented by the independent variables s and f_p , which can be stored inside the array

$$\sigma = [s \quad f_p]^T. \quad (26)$$

3.3. Time-optimal control problem

The aim of time-optimal trajectory planning is to search for the optimal control input $\mathbf{u}(t)$ that grants the trajectory execution in the minimum time (hence minimizing a cost functional), at the same time satisfying the constraints imposed not only on the control $\mathbf{u}(t)$ but also on the state $\mathbf{x}(t)$ that describes the status of the system [26]. The time evolution of the state $\mathbf{x}(t)$ is obtained by integrating the so-called dynamical system, that connects the state $\mathbf{x}(t)$ with the input $\mathbf{u}(t)$ through a system of ordinary differential equations (ODEs). A problem of this type, composed of the minimization of a cost functional, the resolution of the dynamical system, and the fulfillment of some physically meaningful constraints goes under the name of *optimal control problem*.

The jerk of the vector σ is chosen as the control input, in order to ensure smoothness of the trajectory and of the internal force f_p :

$$\mathbf{u} = \ddot{\sigma} = [\ddot{s} \quad \ddot{f}_p]^T. \quad (27)$$

The system state is defined as a vector $\mathbf{x} \in \mathbb{R}^{18}$, namely:

$$\mathbf{x} = [\sigma^T \quad \dot{\sigma}^T \quad \ddot{\sigma}^T \quad \mathbf{q}_l^T \quad \mathbf{q}_r^T]^T, \quad (28)$$

where $\mathbf{q}_l \in \mathbb{R}^6$ and $\mathbf{q}_r \in \mathbb{R}^6$ are the arrays of the robot joint coordinates (Fig. 4).

For the case at hand, the optimal control problem can be formulated as [27,28]:

$$\min_{t_e, \mathbf{u}, f_p} \left[\int_0^{t_e} (1 + k_1 f_p + k_2 \mathbf{u}^T \mathbf{u}) dt \right], \quad (29a)$$

subject to

$$\dot{\mathbf{x}} = \mathbf{f}(\mathbf{x}, \mathbf{u}), \quad (29b)$$

$$\mathbf{x}(0) = [0 \quad f_p(0) \quad 0 \quad 0 \quad 0 \quad 0 \quad \mathbf{q}_l(0)^T \quad \mathbf{q}_r(0)^T]^T, \quad (29c)$$

$$\mathbf{x}(t_e) = [1 \quad f_p(t_e) \quad 0 \quad 0 \quad 0 \quad 0 \quad \mathbf{q}_l(t_e)^T \quad \mathbf{q}_r(t_e)^T]^T, \quad (29d)$$

$$|\dot{\mathbf{q}}_j| \leq \dot{\mathbf{q}}_{j,max} \quad j = l, r, \quad (29e)$$

$$\underline{f}_p \leq f_p \leq \bar{f}_p, \quad (29f)$$

$$\Phi(\{\mathbf{h}_l\}_l, \{\mathbf{h}_r\}_r) \leq \mathbf{0}, \quad (29g)$$

$$|\mathbf{u}| \leq \mathbf{u}_{max}. \quad (29h)$$

The cost functional (29a) is a trade-off between minimal motion time t_e , minimal virtual penetration and minimal jerk. The latter are weighted by the constants k_1 and k_2 , whose values can be conveniently tuned. The function \mathbf{f} in (29b) represents the integration chain of the vector σ from the control \mathbf{u} (30a), and the robot inverse kinematics ((30b), (30c)), namely:

$$\frac{d}{dt} \begin{bmatrix} \sigma \\ \dot{\sigma} \\ \ddot{\sigma} \end{bmatrix} = \begin{bmatrix} \dot{\sigma} \\ \ddot{\sigma} \\ \mathbf{u} \end{bmatrix}, \quad (30a)$$

$$\frac{d}{dt} \mathbf{q}_l = \mathbf{J}_l^{-1} \xi_l(s, \dot{s}), \quad (30b)$$

$$\frac{d}{dt} \mathbf{q}_r = \mathbf{J}_r^{-1} \xi_r(s, \dot{s}). \quad (30c)$$

In (30b) and (30c), the terms $\mathbf{J}_l = \mathbf{J}_l(\mathbf{q}_l)$ and $\mathbf{J}_r = \mathbf{J}_r(\mathbf{q}_r)$ are the Jacobian matrices of the robots, whereas $\xi_l = [\mathbf{r}_{E_l}^T \quad \omega_l^T]^T$ and $\xi_r = [\mathbf{r}_{E_r}^T \quad \omega_r^T]^T$ are the end-effector twists.

The equality constraints ((29c), (29d)) are the initial and final conditions on the state vector \mathbf{x} . The initial and final values of the internal force, namely the 2nd elements of $\mathbf{x}(0)$ and $\mathbf{x}(t_e)$, are not assigned, but the solver is asked to find the values needed to satisfy the inequalities ((24),(25)) in static conditions ($\dot{s} = \ddot{s} = 0$). The values of $\mathbf{q}_j(0)$, with $j = l, r$, are obtained by solving the inverse position analysis of the robots in correspondence of the initial poses of the end-effectors [29]. Conversely, the final values of the joint angles $\mathbf{q}_j(t_e)$ are not precisely assigned, but they are obtained by integration of the inverse kinematics analysis ((30b),(30c)), hence aiding the numerical solution of the optimization. Inequality constraints (29e) consider the limits on the maximum joint velocities $\dot{\mathbf{q}}_{j,max}$ of the robots. The inequality (29f) is used to limit the internal prestress on the object, with \underline{f}_p and \bar{f}_p representing the minimum and the maximum value of f_p , respectively. The constraint (29g) represents the friction conditions ((24),(25)). Inequality (29h) is used to bound the control input, i.e. the jerks of the path parameter and of the internal force.

4. Robot admittance control

The control scheme adopted in this paper is reported in Fig. 5: the same controller is applied to both manipulators. For the sake of clarity, subscripts referring to one or the other robot are omitted. The input is represented by the desired end-effector pose

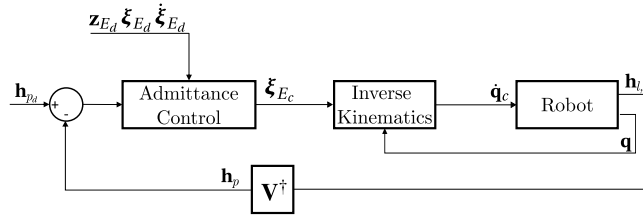


Fig. 5. Admittance control scheme adopted for the dual-arm manipulation.

$\mathbf{z}_d = [\mathbf{r}_{Ed}^T \quad \mathcal{Q}_d^T]^T$ (with \mathcal{Q}_d^T being the quaternion representing the desired rotation matrix \mathbf{R}_d), the end-effector twist $\xi_d = [\dot{\mathbf{r}}_{Ed}^T \quad \dot{\omega}_d^T]^T$, the first-time derivative of the twist $\dot{\xi}_d = [\ddot{\mathbf{r}}_{Ed}^T \quad \ddot{\omega}_d^T]^T$, and the desired internal wrench \mathbf{h}_{pd} . The feedback on the measured end-effector wrenches $\mathbf{h}_{l,r}$ is used to obtain the actual internal wrench \mathbf{h}_p applied on the object, through the expression $\mathbf{h}_p = \mathbf{V}^T \mathbf{h}_{l,r}$ (see Eq. (9)). The error $\Delta \mathbf{h}_p = [\Delta \mathbf{f}_p^T \quad \Delta \mathbf{t}_p^T]^T = \mathbf{h}_{pd} - \mathbf{h}_p$, where $\Delta \mathbf{f}_p = \mathbf{f}_{pd} - \mathbf{f}_p$ and $\Delta \mathbf{t}_p = \mathbf{t}_{pd} - \mathbf{t}_p$ are the force and torque errors, is inserted as input of the admittance-control equations [30]:

$$\mathbf{M}_t \Delta \ddot{\mathbf{r}}_{cd} + \mathbf{D}_t \Delta \dot{\mathbf{r}}_{cd} + \mathbf{K}_t \Delta \mathbf{r}_{cd} = \Delta \mathbf{f}_p, \quad (31a)$$

$$\mathbf{M}_r \Delta \dot{\omega}_{cd} + \mathbf{D}_r \Delta \omega_{cd} + \mathbf{K}_r' \epsilon_{cd} = \Delta \mathbf{t}_p. \quad (31b)$$

Eqs. (31) are expressed in the frame F_j ($j = l, r$) of the corresponding robot end-effector. In (31a), $\Delta \mathbf{r}_{cd} = (\mathbf{r}_{Ec} - \mathbf{r}_{Ed})$, $\Delta \dot{\mathbf{r}}_{cd} = (\dot{\mathbf{r}}_{Ec} - \dot{\mathbf{r}}_{Ed})$, $\Delta \ddot{\mathbf{r}}_{cd} = (\ddot{\mathbf{r}}_{Ec} - \ddot{\mathbf{r}}_{Ed})$ represent the difference between the commanded and the desired end-effector position, velocity and acceleration, respectively. In (31b), the quantities $\Delta \omega_{cd} = \omega_c - \omega_d$, $\Delta \dot{\omega}_{cd} = \dot{\omega}_c - \dot{\omega}_d$ are the differences between the commanded and the desired angular velocity and acceleration of the end-effector. ϵ_{cd} denotes the vectorial part of the quaternion \mathcal{Q}_{cd} extracted from $\mathbf{R}_d^T \mathbf{R}_c$ [30,31] (\mathbf{R}_d and \mathbf{R}_c are the desired and the commanded rotation matrix of the robot end-effector w.r.t. the base frame, respectively). The rotational stiffness \mathbf{K}_r' is [30]

$$\mathbf{K}_r' = 2(\eta_{cd} \mathbf{I} - \tilde{\epsilon}_{cd})^T \mathbf{K}_r, \quad (32)$$

where η_{cd} is the scalar element of quaternion \mathcal{Q}_{cd} .

Matrices $\mathbf{M} = \text{diag}(\mathbf{M}_l \quad \mathbf{M}_r)$, $\mathbf{D} = \text{diag}(\mathbf{D}_l \quad \mathbf{D}_r)$, $\mathbf{K} = \text{diag}(\mathbf{K}_l \quad \mathbf{K}_r)$ are diagonal matrices, whose values can be conveniently tuned to achieve the desired compliant behavior. In particular, \mathbf{M} represents the virtual inertia of the controller, whereas \mathbf{D} and \mathbf{K} reproduce the damping and stiffness desired behavior. Trial-and-error procedures can be performed to obtain the matrix values that grant a reliable tracking of the desired internal wrench and the zeroing of the pose error at the end of the motion. In particular, in this work, we performed translational and rotational motions along and about the axes of the Cartesian frame F_0 , with the object being handled by the two robots, until suitable force and pose tracking were achieved. The following matrices were thus obtained:

$$\mathbf{M}_l = \text{diag}([200 \ 200 \ 50]) \text{ kg}, \quad (33a)$$

$$\mathbf{M}_r = \text{diag}([15 \ 15 \ 15]) \text{ kgm}^2, \quad (33b)$$

$$\mathbf{D}_l = \text{diag}([2400 \ 2400 \ 3600]) \frac{\text{Ns}}{\text{m}}, \quad (33c)$$

$$\mathbf{D}_r = \text{diag}([1200 \ 1200 \ 1200]) \frac{\text{Nms}}{\text{rad}}, \quad (33d)$$

$$\mathbf{K}_l = \text{diag}([500 \ 500 \ 100]) \frac{\text{N}}{\text{m}}, \quad (33e)$$

$$\mathbf{K}_r = \text{diag}([400 \ 400 \ 400]) \frac{\text{Nm}}{\text{rad}}. \quad (33f)$$

The forward integration of the differential equations (31) allows the computation of the commanded end-effector velocity ξ_c , which is transformed in joint space through the robot inverse kinematics, by computing the robot Jacobian matrix $\mathbf{J}(\mathbf{q})$ in correspondence of the actual configuration of the robot joints \mathbf{q} (measured by the encoders). This gives the commanded joint velocities to feed the robot

$$\dot{\mathbf{q}}_c = \mathbf{J}^{-1}(\mathbf{q}) \xi_c. \quad (34)$$

5. Simulation and experiments

5.1. Experimental setup

The experimental setup (depicted in Fig. 6) consists of two UR10 e-Series from Universal Robots, both equipped with an integrated force/torque sensor at the end-effector. Each cobot end-effector is interfaced with a 3D-printed flange, on which a rubbered tape is applied. The manipulated object is a cardboard box with dimensions $200 \times 122 \times 230$ mm and a mass $m_b = 2.022$ kg.

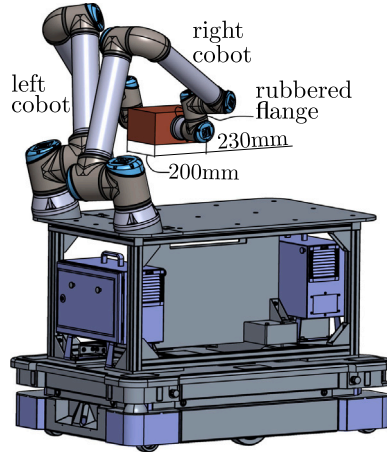


Fig. 6. Illustration of dual-arm setup.

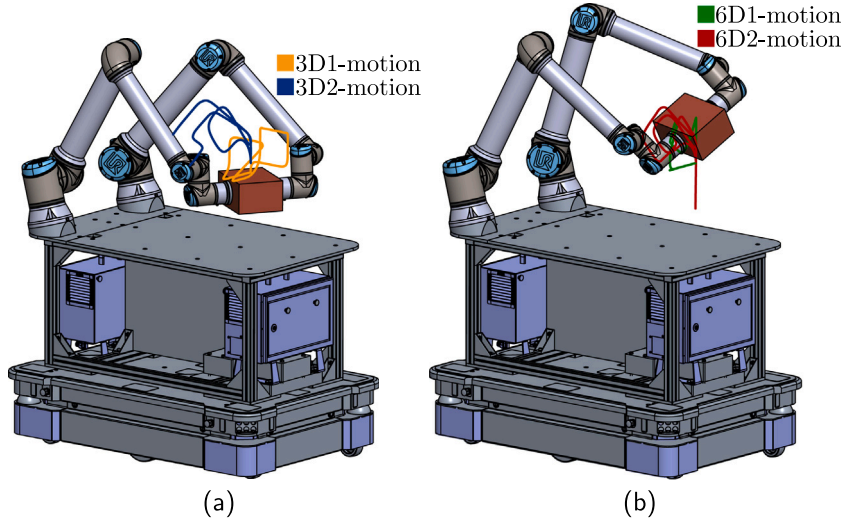


Fig. 7. The four paths prescribed for the dual-arm tests.

The friction coefficient is estimated by an inclined-plane test. The object that has to be manipulated is placed on a rubbered plane, whose inclination can be manually varied thanks to a revolute joint. By acting on the revolute joint in quasi-static conditions, as soon as slipping of the object is detected, the friction angle is read on the angular scale attached to the plane. The static friction between the cardboard and the rubbered flange is hence estimated as $\mu = \tan 28^\circ$.

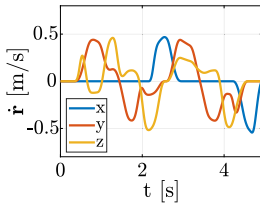
5.2. Time-optimal trajectory planning

In order to solve the time-optimal trajectory planning problem presented in Section 3.3, the values of some parameters must be chosen or identified.

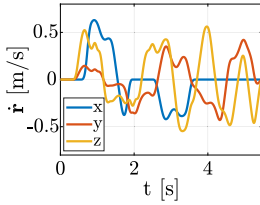
The weights adopted in the cost functional (29a) are chosen equal to $k_1 = 10$ and $k_2 = 0.01$. The two cobots have the same nominal kinematic parameters. In particular, the joint velocity limits used in inequality (29e), obtained from the robot datasheets and adopting a scaling factor equal to 0.5 for the first two joints and to 0.3 for the others, are all set to 1.05 rad/s.

As for the inequality (29f), the maximum and minimum values of the internal prestress are chosen equal to $\bar{f}_p = 50$ N and $\underline{f}_p = 5$ N, respectively. These values are chosen by the user, on the one hand to guarantee a firm grasp, on the other not to damage the manipulated object (depending on the application at hand).

For the function Φ in (29g), a safety factor of 0.9 is enforced: this results in a static friction coefficient used within the optimization equal to $\mu^* = 0.9 \tan 28^\circ = 0.48$. The misalignment of the box COM (see Eq. (16)) along the y direction is assumed to be negligible w.r.t. to the one along the x direction of frame F_l , so that $e_x = 0.03$ m and $e_y = 0$ m. The value of \mathbf{u}_{max} in (29h) is set to $\mathbf{u}_{max} = [5 \text{ s}^{-3} \ 5 \text{ Ns}^{-3}]^T$.

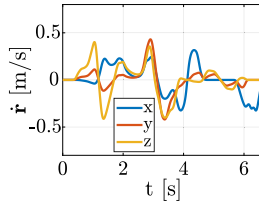


(a)

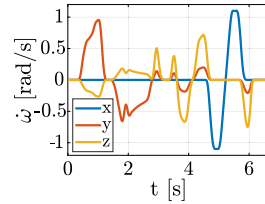


(b)

Fig. 8. Object-velocity profiles for the 3D motions: (a) 3D1-motion; (b) 3D2-motion.



(a)



(b)

Fig. 9. Object-velocity profiles for the 6D motions: (a) 6D1-motion; (b) 6D2-motion.

Fig. 7 shows the four different paths considered for the experiments reported in the paper: the first two (Fig. 7(a)) are purely translational paths, with $\omega = \dot{\omega} = \mathbf{0}$, whereas the two depicted in Fig. 7(b) also involve object rotations ($\omega \neq \mathbf{0}, \dot{\omega} \neq \mathbf{0}$). For the definition of the four paths, the B-spline degree is set to $d = 4$ (v. Eq. (18a)). The trend of the internal prestress f_p , is optimized within the resolution of the constrained problem (29). For each path, two optimizations, that consider different trends of f_p , are carried out:

- the first one imposes a constant optimal value of f_p (which is found by the solver) throughout the whole motion;
- the second one considers a variable optimal f_p (the optimal trend is computed by the solver) during the trajectory execution.

The constrained time-optimal trajectory planning is solved by adopting a multiple-shooting method and using CasADi [32], a software framework implemented in Matlab for nonlinear optimization and optimal control. The problem-solving algorithm is IPOPT [33], which adopts a filter line-search interior-point method.

Figs. 8, 9 show the trends of the object velocity twist, as resulting from the optimization output with a constant f_p (analogous trends apply also for the case of a varying f_p). In Fig. 8, the trend of ω is omitted, being equal to $\mathbf{0}$ throughout the motion. Table 1 reports the maximum values of the norm of the translational and angular velocity and acceleration during the considered motions.

Figs. 10, 11 show the friction conditions obtained by solving the constrained optimization for the 3D1-motion, the 3D2-motion, the 6D1-motion and the 6D2-motion. The first row of each subfigure is related to the contact forces on the left-robot end-effector, whereas the second row refers to the right-robot contact forces. In particular, Fig. 10 illustrates the solution considering a constant value of the internal force f_p , whereas Fig. 11 shows the solution with a varying f_p . In each plot, the blue line shows the absolute values of the normal force $|f_{j,N}|$ acting on the object on the left and right sides of grasping ($j = l, r$), respectively; the purple line indicates the quantity $f_{j,T}/\mu^*$ ($j = l, r$), with $f_{j,T} = \sqrt{f_{j,Tx}^2 + f_{j,Ty}^2}$; the green line represents the quantity $|t_{j,N}|/(\frac{2}{3}\mu^*R)$ ($j = l, r$); the black dashed line denotes the internal prestress f_p . In all plots, the purple line is always under the blue one, indicating that the no-slipping constraint is always satisfied in the modeled scenario. Moreover, the green line is almost always under the purple one, showing that condition (12) is more restrictive than condition (15). The constant value of f_p is optimized according to the motion to be executed; hence, if two different subfigures of Fig. 10 (corresponding to different object motions) are compared, the constant values of f_p are different. Regarding the results of Fig. 11, the obtained varying trends of f_p do not derive from a standard pre-assigned function, but they are computed by the optimization algorithm so as to guarantee that the blue curve lies above the purple and the green curves throughout the motion.

It is worth observing that, in all motions, the object has an acceleration component along the z -axis of frame F_l (i.e. $\ddot{r}_z \neq 0 \text{ m/s}^2$), hence making the normal force being composed of the internal prestress f_p and the inertia force of the object along the z -axis. Depending on the motion direction, the component \ddot{r}_z may help the friction stability on one side of the contact, while it may hinder it on the other side. This can be easily observed in the plots of the 3D motions (Figs. 10(a), 10(b), 11(a), 11(b)) where the blue lines representing the normal forces of the left and right cobots are mirrored w.r.t. the dashed one. The same considerations hold for the 6D motions, where the additional presence of the gravity force along the z -axis of frame F_l makes the mirroring less intelligible.

Fig. 12 shows the ratios between the joint velocities and their maximum values for the right robot, as obtained from the optimization, considering the 6D motions with a constant f_p (the plots of the other cases are similar, so they are skipped for the sake of brevity): the fact that, at some instants, some ratio is equal to 1 shows the achievement of an optimal solution.

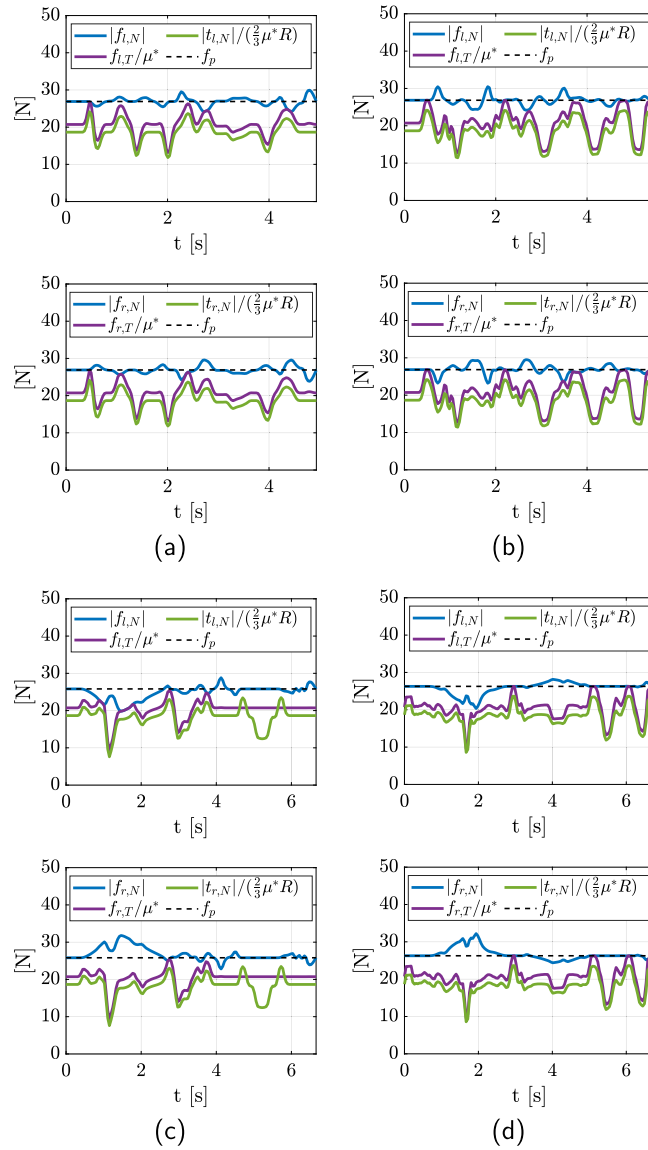


Fig. 10. Optimization results with a constant internal force f_p : (a) 3D1-motion; (b) 3D2-motion; (c) 6D1-motion; (d) 6D2-motion. (For interpretation of the references to color in this figure legend, the reader is referred to the web version of this article.)

Table 1

Maximum values of the velocity and acceleration reached by the manipulated object, as resulting from the optimization.

	Constant f_p	Varying f_p		Constant f_p	Varying f_p
3D1-motion	$ \dot{\mathbf{r}} _{max} = 0.5 \frac{\text{m}}{\text{s}}$	$ \dot{\mathbf{r}} _{max} = 0.5 \frac{\text{m}}{\text{s}}$	6D1-motion	$ \dot{\mathbf{r}} _{max} = 0.6 \frac{\text{m}}{\text{s}}$	$ \dot{\mathbf{r}} _{max} = 0.6 \frac{\text{m}}{\text{s}}$
	$ \ddot{\mathbf{r}} _{max} = 3.6 \frac{\text{m}}{\text{s}^2}$	$ \ddot{\mathbf{r}} _{max} = 3.9 \frac{\text{m}}{\text{s}^2}$		$ \ddot{\mathbf{r}} _{max} = 4.5 \frac{\text{m}}{\text{s}^2}$	$ \ddot{\mathbf{r}} _{max} = 4.5 \frac{\text{m}}{\text{s}^2}$
	$ \dot{\omega} _{max} = 0 \frac{\text{rad}}{\text{s}}$	$ \dot{\omega} _{max} = 0 \frac{\text{rad}}{\text{s}}$		$ \dot{\omega} _{max} = 1.1 \frac{\text{rad}}{\text{s}}$	$ \dot{\omega} _{max} = 1.1 \frac{\text{rad}}{\text{s}}$
	$ \ddot{\omega} _{max} = 0 \frac{\text{rad}}{\text{s}^2}$	$ \ddot{\omega} _{max} = 0 \frac{\text{rad}}{\text{s}^2}$		$ \ddot{\omega} _{max} = 7.4 \frac{\text{rad}}{\text{s}^2}$	$ \ddot{\omega} _{max} = 7.3 \frac{\text{rad}}{\text{s}^2}$
3D2-motion	$ \dot{\mathbf{r}} _{max} = 0.7 \frac{\text{m}}{\text{s}}$	$ \dot{\mathbf{r}} _{max} = 0.7 \frac{\text{m}}{\text{s}}$	6D2-motion	$ \dot{\mathbf{r}} _{max} = 0.6 \frac{\text{m}}{\text{s}}$	$ \dot{\mathbf{r}} _{max} = 0.6 \frac{\text{m}}{\text{s}}$
	$ \ddot{\mathbf{r}} _{max} = 4.5 \frac{\text{m}}{\text{s}^2}$	$ \ddot{\mathbf{r}} _{max} = 4.6 \frac{\text{m}}{\text{s}^2}$		$ \ddot{\mathbf{r}} _{max} = 4.3 \frac{\text{m}}{\text{s}^2}$	$ \ddot{\mathbf{r}} _{max} = 4.3 \frac{\text{m}}{\text{s}^2}$
	$ \dot{\omega} _{max} = 0 \frac{\text{rad}}{\text{s}}$	$ \dot{\omega} _{max} = 0 \frac{\text{rad}}{\text{s}}$		$ \dot{\omega} _{max} = 1.1 \frac{\text{rad}}{\text{s}}$	$ \dot{\omega} _{max} = 1.1 \frac{\text{rad}}{\text{s}}$
	$ \ddot{\omega} _{max} = 0 \frac{\text{rad}}{\text{s}^2}$	$ \ddot{\omega} _{max} = 0 \frac{\text{rad}}{\text{s}^2}$		$ \ddot{\omega} _{max} = 6.6 \frac{\text{rad}}{\text{s}^2}$	$ \ddot{\omega} _{max} = 6.7 \frac{\text{rad}}{\text{s}^2}$

Table 2 summarizes the main results of the optimizations, with an indication of the final time t_e of the corresponding trajectory, together with the initial, maximum and mean values of the obtained internal prestress f_p for each motion. The initial value of f_p is chosen, in every optimization, by the solver in order to satisfy the friction-constraint (12) in static conditions (i.e. $\ddot{\mathbf{r}} = \mathbf{0}$, $\ddot{\omega} = \mathbf{0}$),

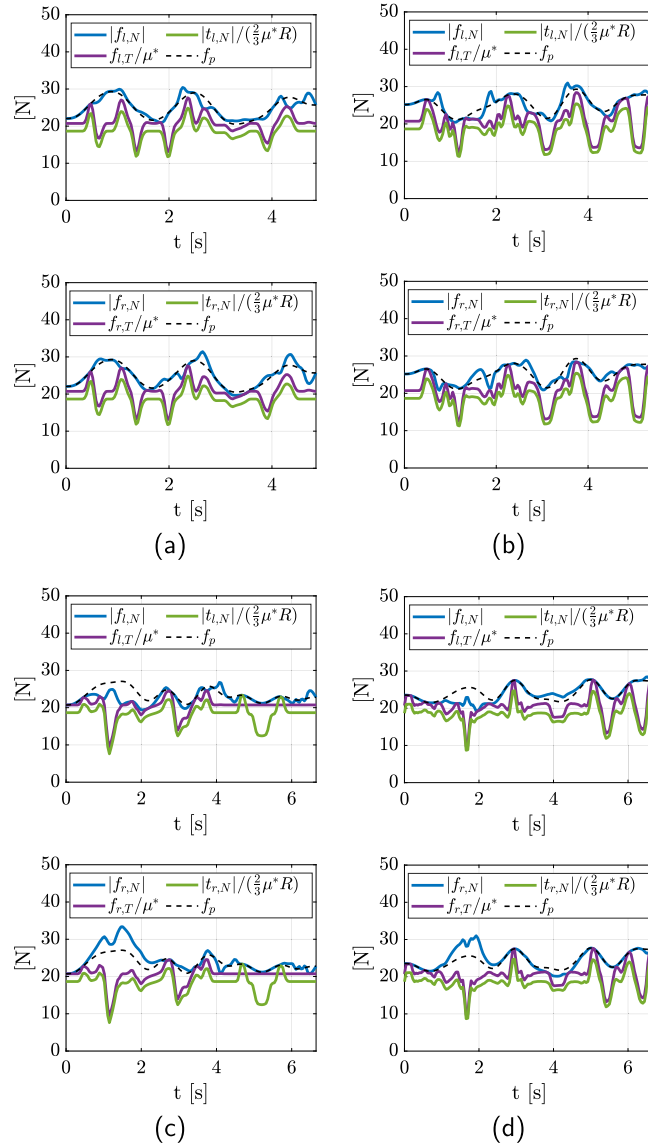


Fig. 11. Optimization results with a varying internal force f_p : (a) 3D1-motion; (b) 3D2-motion; (c) 6D1-motion; (d) 6D2-motion. (For interpretation of the references to color in this figure legend, the reader is referred to the web version of this article.)

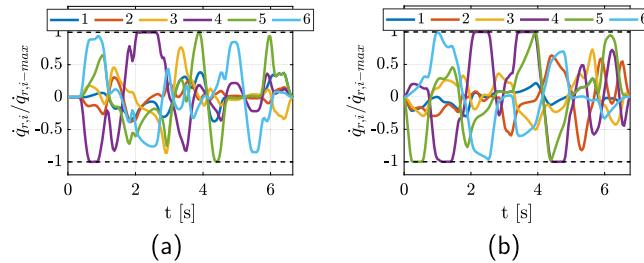
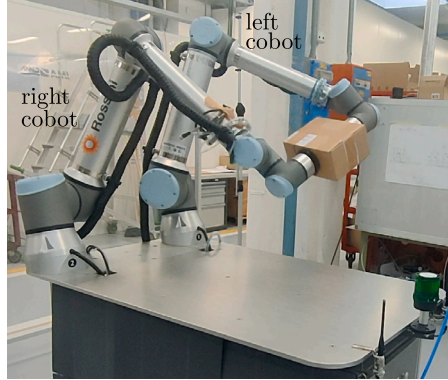


Fig. 12. Ratios between the joint velocities and their maximum values in the optimization results with a constant internal force f_p : (a) 6D1-motion; (b) 6D2-motion.

Table 2

Initial, maximum and mean values of the internal prestress f_p obtained as a result of the time-optimal trajectory planning, with an indication of the final time t_e of the corresponding trajectory.

	Constant f_p	Varying f_p		Constant f_p	Varying f_p
3D1-motion	$t_e = 4.93$ s $f_p(0) = 26.9$ N $f_{p,max} = 26.9$ N $f_{p,med} = 26.9$ N	$t_e = 4.86$ s $f_p(0) = 22.0$ N $f_{p,max} = 29.3$ N $f_{p,med} = 25.0$ N	6D1-motion	$t_e = 6.65$ s $f_p(0) = 25.8$ N $f_{p,max} = 25.8$ N $f_{p,med} = 25.8$ N	$t_e = 6.65$ s $f_p(0) = 20.7$ N $f_{p,max} = 27.1$ N $f_{p,med} = 23.4$ N
3D2-motion	$t_e = 5.47$ s $f_p(0) = 26.8$ N $f_{p,max} = 26.8$ N $f_{p,med} = 26.8$ N	$t_e = 5.44$ s $f_p(0) = 25.2$ N $f_{p,max} = 29.3$ N $f_{p,med} = 25.3$ N	6D2-motion	$t_e = 6.76$ s $f_p(0) = 26.3$ N $f_{p,max} = 26.3$ N $f_{p,med} = 26.3$ N	$t_e = 6.71$ s $f_p(0) = 23.5$ N $f_{p,max} = 27.7$ N $f_{p,med} = 24.3$ N

**Fig. 13.** Experimental dual-arm setup.

namely:

$$f_p(0) \geq \frac{m_b g}{\mu^*}. \quad (35)$$

Looking at Table 2, it can be stated that no apparent advantage in terms of trajectory duration t_e is gained by choosing the optimization with a varying f_p instead of the one with a constant f_p , with the saved time being negligible. Furthermore, for all motions, the maximum value $f_{p,max}$ reached by the internal prestress is slightly higher in the trajectory with a varying f_p w.r.t. the one with a constant internal prestress. Conversely, the trajectory with a varying internal prestress grants a slightly smaller mean value $f_{p,med}$ of the internal prestress.

5.3. Experimental results

The dual-arm setup used during the experiments is shown in Fig. 13. The two cobots are controlled by using ROS, with an admittance-controller node implemented in C++, at a frequency rate of 500 Hz. A transitory procedure of roughly 3 s is executed to bring the prestress to the initial value of $f_p(0)$. The wrenches exerted by the cobots are measured by the integrated 6D force/torque sensors installed inside the end-effector of each UR10 e-Series. These sensors are characterized by a force/torque-measure range of 100 N/10 Nm, with an accuracy of 5.5 N/0.5 Nm, hence not being suitable for accurate force/torque tracking at high dynamics, but suitable to catch reasonably well the force trends.

Figs. 14, 15 show the experimental forces exerted on the object during the 3D1-motion, 3D2-motion, 6D1-motion, and 6D2-motion, respectively. In particular, Fig. 14 depicts the results for the case with a constant value of the internal force f_p , whereas Fig. 15 shows the case with a varying f_p . The forces measured by the left and right sensors are denoted with \hat{f}_l and \hat{f}_r , respectively. The purple line indicates the quantity $|\hat{f}_{j,T}|/\mu$ for the experimental measurement to allow a visual check of the friction-cone condition. The torque readings related to $t_{r,N}$ and $t_{l,N}$ are not reported since, in the reported motions, their maximum values are lower than the sensor accuracy and, thus, the results are too noisy and inconsistent.

Notwithstanding the many non-negligible differences between the modeled and the real scenario (related to the friction model, the dynamical parameters, the force distribution in the over-constrained dual-arm system, the controller errors, the force-sensor errors, etc.), we can see that the experimental trends in Figs. 14 and 15 well catch the simulated ones in Figs. 10 and 11. In particular, the experimental plots show that the blue line is always over the purple one (except for some isolated time instants, which must not be interpreted in a strict way, due to the aforementioned errors), hence confirming that friction inequalities are

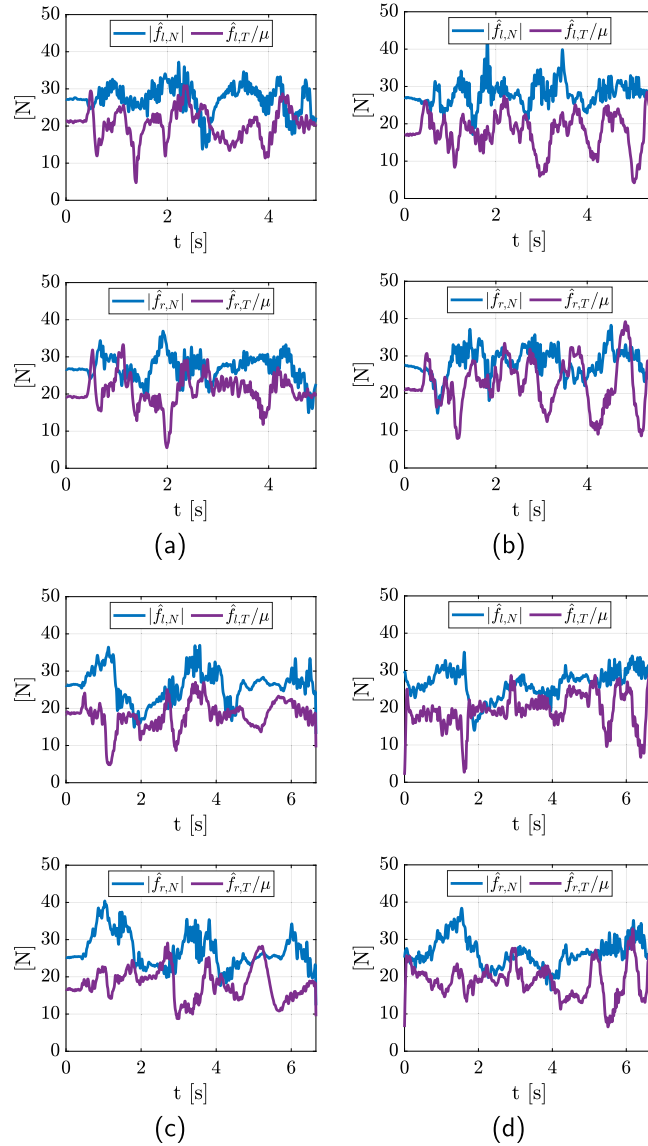


Fig. 14. Assessment of the friction-cone condition with a constant internal force f_p : (a) 3D1-motion; (b) 3D2-motion; (c) 6D1-motion; (d) 6D2-motion. (For interpretation of the references to color in this figure legend, the reader is referred to the web version of this article.)

respected during trajectory execution. This also finds evidence by looking at the Video 1,¹ where no slipping of the object occurs, even when the box is tilted around the z-axis of F_l .

Table 3 reports the force accuracy indexes $\varepsilon_{j,max}$ and $\varepsilon_{j,med}$, defined as

$$\varepsilon_{j,max} = \frac{|f_{j,N}|_{max-exp} - |f_{j,N}|_{max-mod}}{|f_{j,N}|_{max-mod}} \times 100\%, \quad (36)$$

$$\varepsilon_{j,med} = \frac{|f_{j,N}|_{med-exp} - |f_{j,N}|_{med-mod}}{|f_{j,N}|_{med-mod}} \times 100\%, \quad (37)$$

¹ A video of the performed dual-arm motions is available as a supplementary material.

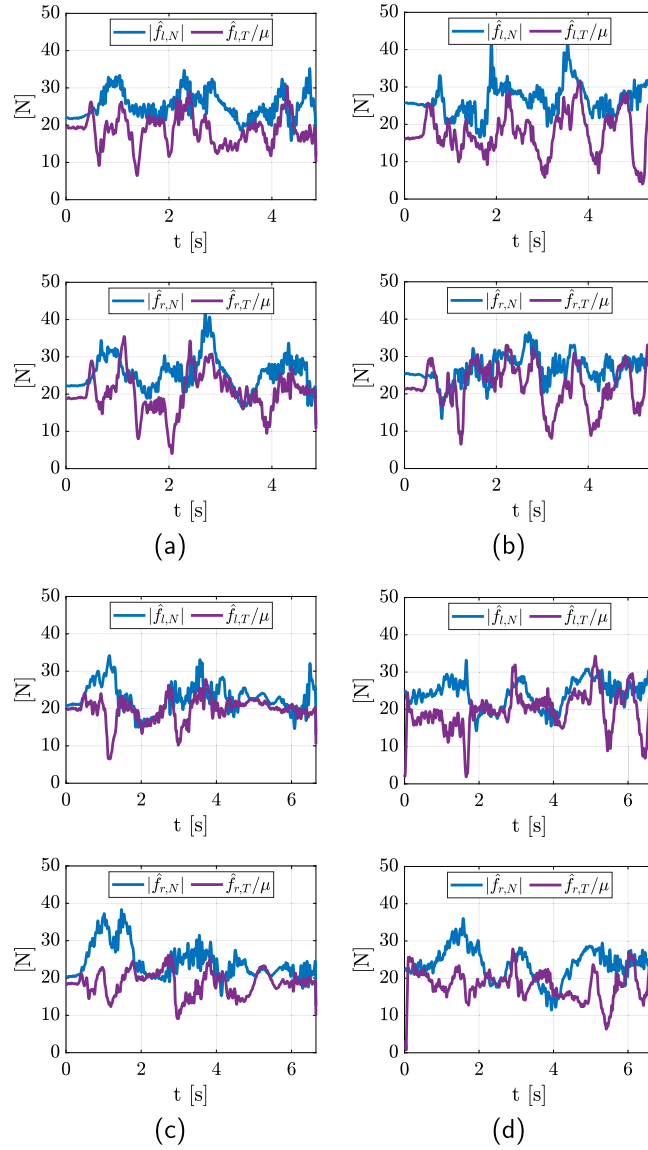


Fig. 15. Assessment of the friction-cone condition with a varying internal force f_p : (a) 3D1-motion; (b) 3D2-motion; (c) 6D1-motion; (d) 6D2-motion. (For interpretation of the references to color in this figure legend, the reader is referred to the web version of this article.)

Table 3
Normal force accuracy indexes.

	Constant f_p	Varying f_p		Constant f_p	Varying f_p
3D1-motion	$\epsilon_{l,max} = 24.1\%$	$\epsilon_{l,max} = 15.6\%$	6D1-motion	$\epsilon_{l,max} = 28.0\%$	$\epsilon_{l,max} = 27.0\%$
	$\epsilon_{l,med} = 1.8\%$	$\epsilon_{l,med} = 1.0\%$		$\epsilon_{l,med} = -0.3\%$	$\epsilon_{l,med} = 1.5\%$
	$\epsilon_{r,max} = 24.7\%$	$\epsilon_{r,max} = 33.3\%$		$\epsilon_{r,max} = 28.6\%$	$\epsilon_{r,max} = 14.7\%$
	$\epsilon_{r,med} = 0.8\%$	$\epsilon_{r,med} = 2.7\%$		$\epsilon_{r,med} = -3.6\%$	$\epsilon_{r,med} = -0.35\%$
3D2-motion	$\epsilon_{l,max} = 44.2\%$	$\epsilon_{l,max} = 42.3\%$	6D2-motion	$\epsilon_{l,max} = 24.0\%$	$\epsilon_{l,max} = 16.5\%$
	$\epsilon_{l,med} = 4.6\%$	$\epsilon_{l,med} = 5.6\%$		$\epsilon_{l,med} = 2.5\%$	$\epsilon_{l,med} = 1.5\%$
	$\epsilon_{r,max} = 29.5\%$	$\epsilon_{r,max} = 26.0\%$		$\epsilon_{r,max} = 19.1\%$	$\epsilon_{r,max} = 16.2\%$
	$\epsilon_{r,med} = 5.2\%$	$\epsilon_{r,med} = 5.9\%$		$\epsilon_{r,med} = -0.5\%$	$\epsilon_{r,med} = -3.3\%$

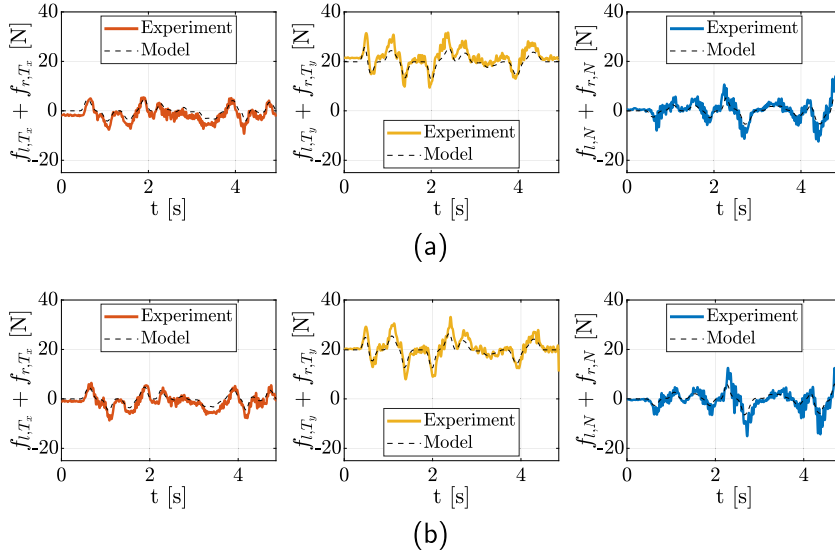


Fig. 16. Assessment on the application of the net wrench on the object and the gripper for the 3D1-motion: (a) Constant internal force f_p ; (b) Varying internal force f_p .

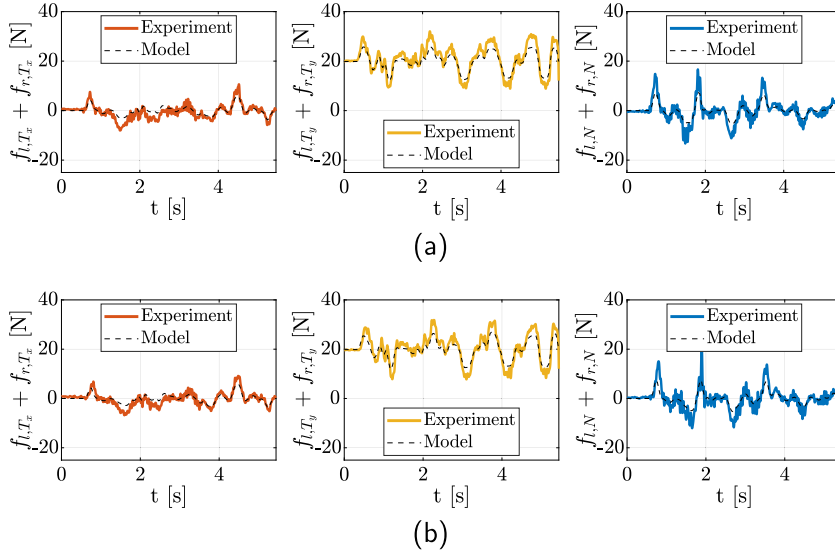


Fig. 17. Assessment on the application of the net wrench on the object and the gripper for the 3D2-motion: (a) Constant internal force f_p ; (b) Varying internal force f_p .

where *mod* and *exp* denote the model and the experimental quantities, and $|f_{j,N}|_{med-p}$ ($p = exp, mod$) is the mean value of $f_{j,N}$ ($j = l, r$) during the motion time period, namely

$$|f_{j,N}|_{med-p} = \frac{\sum_{i=1}^{N_{tot}} |f_{j,N,p}(t_i)|}{N_{tot}}, \quad j = l, r, \quad (38)$$

with N_{tot} being the total number of samples. The force accuracy indexes $\varepsilon_{j,max}$ and $\varepsilon_{j,med}$ in Eqs. (36) and (37) are used to assess the effectiveness of the implemented admittance control in exerting the desired normal forces (including the commanded internal force f_p - see (11)) on the object by both robots. It can be noted that, in most cases, for a given motion type, the trajectory with a varying f_p grants lower values of the accuracy indexes $\varepsilon_{j,max}$ and $\varepsilon_{j,med}$ ($j = l, r$), w.r.t. the case with a constant f_p . Furthermore, the value of $\varepsilon_{j,med}$ is always below 5.9%, proving that the general trend of the normal forces exerted on the object remains in line with the commanded trend, even when the percentage error of the maxima $\varepsilon_{j,max}$ is high.

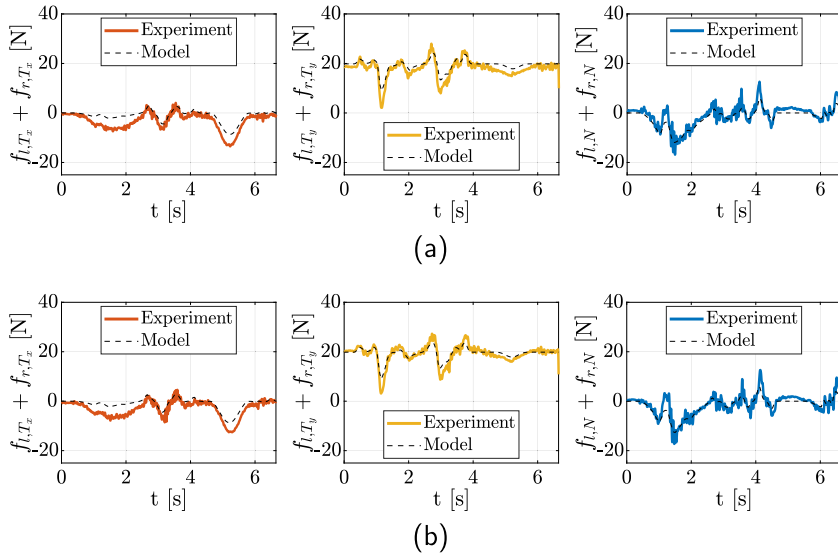


Fig. 18. Assessment on the application of the net wrench on the object and the gripper for the 6D1-motion: (a) Constant internal force f_p ; (b) Varying internal force f_p .

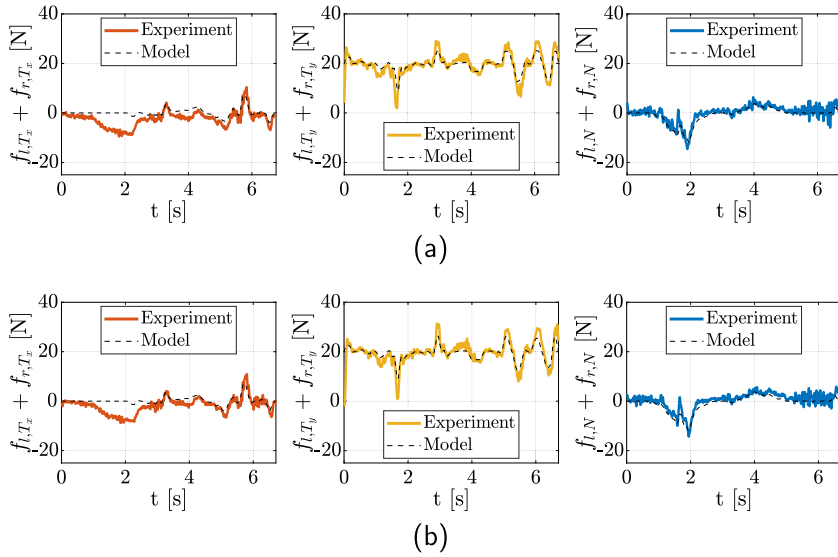


Fig. 19. Assessment on the application of the net wrench on the object and the gripper for the 6D2-motion: (a) Constant internal force f_p ; (b) Varying internal force f_p .

Figs. 16, 17, 18, 19 illustrate, for each motion, with both a constant and a varying f_p , the sum of the reaction forces \mathbf{f}_l and \mathbf{f}_r , projected on the coordinate frame F_l . Recalling Eq. (2a), this sum only depends on the motion law and, thus, is not affected by our subjective choices related to force distributions. In each subfigure, the left-most plot displays the sum $f_{l,T_x} + f_{r,T_x}$, the central plot the sum $f_{l,T_y} + f_{r,T_y}$ and the right-most plot reports the quantity $f_{l,N} + f_{r,N}$. In particular, the colored solid lines indicate the experimental trends, and the black dashed lines are the model predictions. The good correspondence between the model and the experiment demonstrates that the net force exerted by the cobots on the object and the gripper equals the desired dynamics.

6. Conclusions

This paper studied the unilateral cooperative grasping of an object manipulated by two robots. The peculiarity of this manipulation strategy is that no grippers are used, but the object is held by means of unilateral contact forces, while performing highly dynamical motions and, at the same time, ensuring that no slipping occurs. The internal force exerted along the contact normal

between the cobot end-effectors and the object was included within the inputs of a constrained time-optimal trajectory-planning problem, aimed at minimizing both the trajectory duration and the contact forces. In particular, an optimized constant value and an optimized varying trend of the internal force were considered. Several 6D motions were performed in a real scenario by employing two collaborative robots, which were admittance-controlled.

An extensive validation campaign showed that no slipping of the object occurred even considering fast motions (with a maximum acceleration and angular acceleration of 4.5 m/s^2 and 7.4 rad/s^2 , respectively), hence advancing the state of the art. The correct wrench application on the object was confirmed by force and torque measurements, thus ensuring that the object followed the desired trajectory and respected the static-friction conditions ensuring no slipping. A quantitative analysis was reported, highlighting that the force accuracy indexes regarding the application of a suitable normal force were always under an acceptable threshold. No major differences emerged between the cases corresponding to a constant or a variable optimal internal force, though the latter seemed to grant a slightly more reliable tracking of the commanded normal force and a smaller average prestress on the object.

Further developments will see a more detailed tuning campaign of the admittance-control matrices, also making them vary with the robot configurations [34]. This would eventually improve the control of the normal-force application. In addition, a deeper investigation on the force distribution will be addressed to better capture the trends of the tangential forces, especially during orientation-changing motions [35,36]. As far as the trajectory-optimization method is concerned, the study of the robustness of the algorithm w.r.t. inertia-parameter uncertainties and the application of external disturbances on the manipulated object [37] will be the object of future work. Finally, point-to-point motions (in which only the initial and final poses are assigned) will be considered to release the object from following a prescribed path. This approach can be pursued offline, by making the optimization algorithm find the shortest path to be followed in minimal time and fulfilling the friction-cone conditions, also taking into account collision-avoidance constraints [38,39].

CRedit authorship contribution statement

Roberto Di Leva: Writing – review & editing, Writing – original draft, Validation, Software, Investigation, Data curation, Conceptualization. **Hubert Gattringer:** Writing – review & editing, Supervision, Conceptualization. **Andreas Müller:** Supervision, Project administration, Conceptualization. **Marco Carricato:** Writing – review & editing, Supervision, Project administration, Methodology, Conceptualization.

Declaration of competing interest

The authors declare that they have no known competing financial interests or personal relationships that could have appeared to influence the work reported in this paper.

Data availability

Data will be made available on request.

Acknowledgments

The authors would like to express their gratitude to the IMA R&D Department for providing the hardware and the setup needed to perform the experiments. This work was funded under the National Recovery and Resilience Plan (NRRP), Mission 04 Component 2 Investment 1.5—NextGenerationEU, Call for tender n. 3277 dated 30 December 2021 Award Number: 0001052 dated 23 June 2022. This work was also partially supported by the “LCM-K2 Center for Symbiotic Mechatronics, Austria” within the framework of the Austrian COMET-K2 program.

Appendix A. Supplementary data

Supplementary material related to this article can be found online at <https://doi.org/10.1016/j.mechmachtheory.2024.105729>.

References

- [1] S. Makris, P. Tsarouchi, A.-S. Mattheiakias, A. Athanasatos, X. Chatzigeorgiou, M. Stefanos, K. Giavridis, S. Aivaliotis, Dual arm robot in cooperation with humans for flexible assembly, *CIRP Ann* 66 (1) (2017) 13–16, <http://dx.doi.org/10.1016/j.cirp.2017.04.097>.
- [2] S. Makris, Cooperative manipulation—The case of dual arm robots, in: *Cooperating Robots for Flexible Manufacturing*, Springer International Publishing, 2020, pp. 123–132, http://dx.doi.org/10.1007/978-3-030-51591-1_5.
- [3] M. Garabini, D. Caporale, V. Tincani, A. Palleschi, C. Gabellieri, M. Gugliotta, A. Settimi, M.G. Catalano, G. Grioli, L. Pallottino, WRAPP-up: A dual-arm robot for intralogistics, *IEEE Robot. Autom. Mag.* 28 (3) (2021) 50–66, <http://dx.doi.org/10.1109/mra.2020.3015899>.
- [4] C. Smith, Y. Karayiannidis, L. Nalpantidis, X. Gratal, P. Qi, D.V. Dimarogonas, D. Kragic, Dual arm manipulation—A survey, *Robot. Auton. Syst.* 60 (10) (2012) 1340–1353, <http://dx.doi.org/10.1016/j.robot.2012.07.005>.
- [5] R. Bonitz, T. Hsia, Force decomposition in cooperating manipulators using the theory of metric spaces and generalized inverses, in: *1994 IEEE International Conference on Robotics and Automation*, San Diego, CA, USA, 1994, pp. 1521–1527, <http://dx.doi.org/10.1109/robot.1994.351372>.
- [6] R. Bonitz, T. Hsia, Robust dual-arm manipulation of rigid objects via palm grasping-theory and experiments, in: *Proceedings of IEEE International Conference on Robotics and Automation*, Minneapolis USA, IEEE, 1996, pp. 3047–3054, <http://dx.doi.org/10.1109/robot.1996.509175>.

- [7] D.S. Carabis, J.T. Wen, Slip avoidance in dual-arm manipulation, in: 2018 IEEE/RSJ International Conference on Intelligent Robots and Systems, IROS, Madrid, Spain, IEEE, 2018, pp. 2872–2879, <http://dx.doi.org/10.1109/iros.2018.8593377>.
- [8] M. Schumacher, J. Wojtusich, P. Beckerle, O. von Stryk, An introductory review of active compliant control, *Robot. Auton. Syst.* 119 (2019) 185–200, <http://dx.doi.org/10.1016/j.robot.2019.06.009>.
- [9] M.T. Mason, Compliance and force control for computer controlled manipulators, *IEEE Trans. Syst. Man Cybern.* 11 (6) (1981) 418–432, <http://dx.doi.org/10.1109/tsmc.1981.4308708>.
- [10] S. Chilverini, L. Sciacivco, The parallel approach to force/position control of robotic manipulators, *IEEE Trans. Robot. Autom.* 9 (4) (1993) 361–373, <http://dx.doi.org/10.1109/70.246048>.
- [11] N. Hogan, Impedance control: An approach to manipulation: Part I—theory, *J. Dyn. Syst. Meas. Control* 107 (1) (1985) 1–7, <http://dx.doi.org/10.1115/1.3140702>.
- [12] B. Chen, Y. Wang, P. Lin, A hybrid control strategy for dual-arm object manipulation using fused force/position errors and iterative learning, in: 2018 IEEE/ASME International Conference on Advanced Intelligent Mechatronics, AIM, Auckland, New Zealand, 2018, pp. 39–44, <http://dx.doi.org/10.1109/AIM.2018.8452248>.
- [13] F. Caccavale, P. Chiacchio, A. Marino, L. Villani, Six-DOF impedance control of dual-arm cooperative manipulators, *IEEE/ASME Trans. Mechatronics* 13 (5) (2008) 576–586, <http://dx.doi.org/10.1109/TMECH.2008.2002816>.
- [14] H. Sadeghian, F. Ficuciello, L. Villani, M. Keshmiri, Global impedance control of dual-arm manipulation for safe interaction, *IFAC Proc. Vol.* 45 (22) (2012) 767–772, <http://dx.doi.org/10.3182/20120905-3-HR-2030.00154>.
- [15] M. Bjerkeng, J. Schrimpf, T. Myhre, K.Y. Pettersen, Fast dual-arm manipulation using variable admittance control: Implementation and experimental results, in: 2014 IEEE/RSJ International Conference on Intelligent Robots and Systems, IROS, Chicago, IL, USA, 2014, pp. 4728–4734, <http://dx.doi.org/10.1109/iros.2014.6943235>.
- [16] D. Kaserer, H. Gatringer, A. Müller, Time optimal motion planning and admittance control for cooperative grasping, *IEEE Robot. Autom. Lett.* 5 (2) (2020) 2216–2223, <http://dx.doi.org/10.1109/LRA.2020.2970644>.
- [17] H. Haghsheenas, A. Hansson, M. Norrlöf, Time-optimal path tracking for cooperative manipulators: A convex optimization approach, *Control Eng. Pract.* 140 (2023) 105668, <http://dx.doi.org/10.1016/j.conengprac.2023.105668>.
- [18] C. Wang, X. Zang, X. Zhang, Y. Liu, J. Zhao, Parameter estimation and object gripping based on fingertip force/torque sensors, *Measurement* 179 (2021) 109479, <http://dx.doi.org/10.1016/j.measurement.2021.109479>.
- [19] Y. Yu, T. Arima, S. Tsujio, Estimation of object inertia parameters on robot pushing operation, in: Proceedings of the 2005 IEEE International Conference on Robotics and Automation, IEEE, <http://dx.doi.org/10.1109/robot.2005.1570351>.
- [20] B. Siciliano, L. Sciacivco, L. Villani, G. Oriolo, *Robotics: Modelling, planning and control*, Springer London, 2009, pp. 1–623.
- [21] I.D. Walker, R.A. Freeman, S.I. Marcus, Analysis of motion and internal loading of objects grasped by multiple cooperating manipulators, *Int. J. Robot. Res.* 10 (4) (1991) 396–409, <http://dx.doi.org/10.1177/027836499101000408>.
- [22] R.D. Howe, M.R. Cutkosky, Practical force-motion models for sliding manipulation, *Int. J. Robot. Res.* 15 (6) (1996) 557–572, <http://dx.doi.org/10.1177/027836499601500603>.
- [23] A. Bicchi, C. Melchiorri, D. Balluchi, On the mobility and manipulability of general multiple limb robots, *IEEE Trans. Robot. Autom.* 11 (2) (1995) 215–228, <http://dx.doi.org/10.1109/70.370503>.
- [24] L. Piegl, W. Tiller, *The NURBS Book*, Springer Berlin, 1995.
- [25] L. Biagiotti, C. Melchiorri, *Trajectory planning for automatic machines and robots*, Springer Berlin, 2009, pp. 1–514, <http://dx.doi.org/10.1007/978-3-540-85629-0>.
- [26] A. Reiter, *Optimal Path and Trajectory Planning for Serial Robots*, Springer Fachmedien Wiesbaden, 2020, <http://dx.doi.org/10.1007/978-3-658-28594-4>.
- [27] R. Di Leva, M. Carricato, H. Gatringer, A. Müller, Time-optimal trajectory planning for anti-sloshing 2-dimensional motions of an industrial robot, in: 2021 20th International Conference on Advanced Robotics (ICAR), Ljubljana, Slovenia, 2021, pp. 32–37, <http://dx.doi.org/10.1109/icar53236.2021.9659383>.
- [28] H. Gatringer, A. Müller, M. Oberherber, D. Kaserer, Time-optimal path following for robotic manipulation of loosely placed objects: Modeling and experiment, *IFAC-PapersOnLine* 53 (2) (2020) 8450–8455, <http://dx.doi.org/10.1016/j.ifacol.2020.12.1433>.
- [29] L.-T. Schreiber, C. Gosselin, Determination of the inverse kinematics branches of solution based on joint coordinates for universal robots-like serial robot architecture, *ASME J. Mech. Robot.* 14 (3) (2021) 034501, <http://dx.doi.org/10.1115/1.4052805>.
- [30] F. Caccavale, C. Natale, B. Siciliano, L. Villani, Six-DOF impedance control based on angle/axis representations, *IEEE Trans. Robot. Autom.* 15 (2) (1999) 289–300, <http://dx.doi.org/10.1109/70.760350>.
- [31] D. Kaserer, H. Gatringer, A. Müller, Admittance control of a redundant industrial manipulator without using force/torque sensors, in: IECON 2016 - 42nd Annual Conference of the IEEE Industrial Electronics Society, Florence, Italy, 2016, pp. 5310–5315, <http://dx.doi.org/10.1109/IECON.2016.7794088>.
- [32] J. Andersson, J. Gillis, G. Horn, J. Rawlings, M. Diehl, CasADi: A software framework for nonlinear optimization and optimal control, *Math. Program. Comput.* 11 (2019) 1–36, <http://dx.doi.org/10.1007/s12532-018-0139-4>.
- [33] A. Wächter, L.T. Biegler, On the implementation of an interior-point filter line-search algorithm for large-scale nonlinear programming, *Math. Program.* 106 (1) (2005) 25–57, <http://dx.doi.org/10.1007/s10107-004-0559-y>.
- [34] Y. Zhou, Z. Li, Y. Li, M. Zhu, Neural network-based variable stiffness impedance control for internal/external forces tracking of dual-arm manipulators under uncertainties, *Control Eng. Pract.* 141 (2023) 105714, <http://dx.doi.org/10.1016/j.conengprac.2023.105714>.
- [35] T. Watanabe, T. Yoshikawa, Grasping optimization using a required external force set, *IEEE Trans. Autom. Sci. Eng.* 4 (1) (2007) 52–66, <http://dx.doi.org/10.1109/tase.2006.873005>.
- [36] S. Erhart, S. Hirche, Internal force analysis and load distribution for cooperative multi-robot manipulation, *IEEE Trans. Robot.* 31 (5) (2015) 1238–1243, <http://dx.doi.org/10.1109/tro.2015.2459412>.
- [37] L. Chen, L.F.C. Figueredo, M.R. Dogar, Manipulation planning under changing external forces, *Auton. Robots* 44 (7) (2020) 1249–1269, <http://dx.doi.org/10.1007/s10514-020-09930-z>.
- [38] A. Völz, K. Graichen, An optimization-based approach to dual-arm motion planning with closed kinematics, in: 2018 IEEE/RSJ International Conference on Intelligent Robots and Systems, IROS, Madrid, Spain, 2018, pp. 8346–8351, <http://dx.doi.org/10.1109/IROS.2018.8593927>.
- [39] D. Kaserer, H. Gatringer, A. Müller, M. Neubauer, Optimal point-to-point trajectory planning with collision avoidance for dual arm setup, in: 2017 8th ECCOMAS Thematic Conference on MULTIBODY DYNAMICS, Prague, Czech Republic, 2017, pp. 645–654.